

Ferroelectric domain wall motion in freestanding single-crystal complex oxide thin film

*Saidur R. Bakaul**, Jaegyu Kim, Seungbum Hong, Mathew J. Cherukara, Tao Zhou, Liliana Stan, Claudy R. Serrao, Sayeef Salahuddin, Amanda K. Petford-Long, Dillon D. Fong, Martin V. Holt

Dr. S. R. Bakaul, Dr. A. K. Petford-Long, Dr. D. D. Fong
Materials Science Division
Argonne National Laboratory
Lemont, IL 60439, USA
Email: sbakaul@anl.gov

J. Kim, Prof. S. Hong
Department of Materials Science and Engineering
Korea Advanced Institute of Science and Technology (KAIST)
Daejeon, 34141, Republic of Korea

Dr. M. J. Cherukara, Dr. T. Zhou, L. Stan, Dr. M. V. Holt
Center for Nanoscale Materials
Argonne National Laboratory
Lemont, IL 60439, USA

Dr. C. R. Serrao, Prof. S. Salahuddin
Electrical Engineering & Computer Sciences
University of California
Berkeley, CA 94720, USA

Keywords: (Freestanding, single-crystal, complex oxide, ferroelectric, domain walls)

Abstract. Ferroelectric domain walls in single-crystal complex oxide thin films are found to be orders of magnitude slower when the interfacial bonds with the heteroepitaxial substrate are broken to create a freestanding film. This drastic change in domain wall kinetics does not originate from the alteration of epitaxial strain, rather it is correlated with the structural ripples at mesoscopic length scale and associated flexoelectric effects induced in the freestanding films. In contrast, the effects of the bond-breaking on the local static ferroelectric properties of both top and bottom layers of the freestanding films, such as domain wall width and spontaneous polarization are modest and governed by the change in epitaxy-induced compressive strain.

Single-crystal complex oxide ferroelectric (FE) thin films exhibit high spontaneous polarization, coherent switching and low coercive field – a unique set of properties ideal for the manufacture of energy-efficient, beyond-CMOS logic and memory components,^[1] as well as future quantum computing devices.^[2] One of the primary bottlenecks in this field stems from the great difficulty in producing high quality interfaces between these single-crystal oxides and the single-crystal silicon - the prevalent substrate in microelectronics, hindering their widespread use. Recent developments in complex oxide layer transfer techniques (LTTs), however, may make the monolithic integration of not only FE materials possible^[3,4] but also other single-crystal functional oxides such as half-metals, high T_c superconductors and multiferroic materials - even down to monolayer thickness.^[5-10] As such, LTTs offer an extremely promising alternative to direct growth techniques^[11] in terms of novel device fabrication. In most LTTs, complex oxides are epitaxially grown on a lattice-matched substrate, are made freestanding, and are then interfaced with a different material. Although proof-of-concept, electrostatically-controlled transistors and two-terminal memory devices have already been demonstrated using such transferred complex oxide FE layers,^[3,4] much remains unknown regarding their ferroic properties, particularly at the mesoscopic length scale. This is a necessary step towards integration of these unique materials into microelectronic devices which often utilize sub-100 nm functional features.

Recent studies have reported that freestanding complex oxide thin films exhibit physical properties significantly different from the original, as-grown films. For instance, the collapse of crystalline order has been reported in ultrathin, freestanding STO layers, induced by the electron-volt-level energy of bond breaking that is released from the interfacial layer during the transfer process.^[5] How such an energy landscape and bond rearrangement in one layer would necessarily affect the other layers of a single crystal complex oxide thin film, *i.e.*, in a three-dimensional object, is poorly understood. Unlike 2D materials such as graphene, the complex oxides have strong interlayer bonds, which allows for long range, three-dimensional mechanical

energy propagation.^[12] The interfacial bond energy in typical complex oxide heterostructures is quite high and therefore, atomistic changes at the interface will alter the properties of all the layers, resulting in a very different mechanical and electrostatic energy landscape in the entirety of the material.

In this work, we study the effect of interfacial bond-breaking on the dynamic and static behavior of FE domain walls, as well as the local structural properties. In particular, we probe the bottom surface of the transferred films (denoted as *bottom layers*) that were interfaced with the substrate during growth. We investigate domain wall (DW) motion and width, local capacitance, spontaneous polarization and structural properties using piezoresponse force microscopy (PFM),^[13] electrostatic force microscopy (EFM),^[14] microwave impedance microscopy^[15] and synchrotron X-ray nanodiffraction^[16]. The nominal radii of both the scanning probe microscopy (SPM) and X-ray probes used here range from 20-30 nm, allowing the determination of material properties on a length scale relevant to DW motion. From these studies, we make two key findings: 1) interfacial bond-breaking reduces the DW velocity by 2–3 orders of magnitude, and 2) interfacial bond-breaking allows the compressively-strained layers to attain the strain-free bulk state but introduces subtle structural “ripples” within the layers. We claim that the induced structural inhomogeneity affects DW motion more strongly than the change in strain. However, the static properties, even at the bottom layers, are found to be minimally changed and mostly governed by the reduction of compressive strain.

Figure 1a-c show schematics of the complex oxide layers and measurement setup. The as-grown samples are 40 and 100-nm-thick $\text{PbZr}_{0.2}\text{Ti}_{0.8}\text{O}_3$ (PZT) films, epitaxially synthesized by pulsed laser deposition onto a 10-nm-thick $\text{La}_{0.7}\text{Sr}_{0.3}\text{MnO}_3$ (LSMO) / SrTiO_3 (001) substrate. The same samples were used to derive the transferred layers using the LTT. The freestanding samples were transferred in an upside-down fashion onto a similar LSMO/STO substrate, allowing the scanning probe microscope (SPM) to probe the DW velocity and static ferroic properties of the bottom layers.

To measure the DW velocity, we switched domain polarities in a pre-poled area using the SPM tip as the top electrode and the LSMO film as the bottom electrode. A pulsed electric field was applied across the FE layers, resulting in circular-domains with 40-180 nm radius (R) (**Figure 2a, b**). As the pulse duration was increased ($t = 2 - 2 \times 10^5 \mu\text{s}$), the DWs moved laterally, and domain size increased in a semi-logarithmic fashion. The domain sizes in the transferred samples were much smaller than those in the as-grown samples for the same duration of pulse. Furthermore, the DWs in the transferred samples needed slightly longer pulses to initiate movement compared to the as-grown samples, which suggests the presence of an additional energy barrier in the transferred samples.

We estimate the lateral velocity of the walls from the correlation between the time difference between two successive pulses and resulting increment in domain size.^[17] As shown in Figure 2d and Figure 2e, the wall velocity scales logarithmically with inverse electric field (E) along the direction of DW motion, as expected from the Merz's law of DW creep.^[17-21] We find that the presence of the additional energy barrier in all of the transferred samples hinders DW movement and results in orders of magnitude smaller velocity compared to the as-grown samples. Similar DW kinetics are observed in the top layers of the freestanding film, indicating that interfacial bond-breaking affects the DW kinetics throughout the thickness of the PZT (Figure S1a,b, Supporting Information). Interestingly, the bond-breaking results in stronger impedance to DW motion in thinner films than the thicker films, as reflected in Figure 2d and Figure 2e.

The energy barrier that the DWs need to overcome to move depends on the energy density of both the wall and the nucleated domain. This activation energy is mainly determined by spontaneous polarization density (P_s), DW width (W) and lattice spacing (b) of the material.^[22,23] We measured P_s by monitoring the electrostatic interaction between a DC-biased oscillating probe and the surface charge density, which results in phase shift ($\Delta\phi$) proportional to the polarization.^[24] We find that P_s reduces by only $3 \pm 2 \mu\text{C}/\text{cm}^2$ (2–10%) after transferring

the PZT layers (**Figure 3a-c** and **S2**, Supporting Information). Such a small difference in the spontaneous polarization density corresponds to negligible FE dead layer at the bottom surface of the PZT film. This suggests that intrinsic dead layers ^[25,26] may not be a limiting factor for utilizing transferred epitaxial layers in electrostatically-controlled devices. From the PFM measurement, we also find that the DWs in the transferred samples are slightly wider than in the as-grown films (**Figure 3d** and **Figure S2** and section **S4** of Supporting Information). A broader wall is an indication that the order parameter can fluctuate easily with a lower energy cost, and therefore the susceptibility, which is a measure of the softness of the order parameter, is expected to be high in the transferred PZT. Simulated susceptibilities considering strain change in the films are in agreement with this prediction (**S4**, Supporting Information).

Due to the small tip-sample contact area and ambient electromagnetic interference, measurement of and comparison between local susceptibilities of different samples is beyond our instrumentation capability. Nevertheless, we probed the qualitative behavior of local capacitance changes during polarization reversal process using a scanning microwave impedance microscopy (SMIM) technique with sweeping dc voltage. This provides information about the electronic energy landscape of the material through which the DWs move. **Figure 3e** and **3f** show the change in capacitive current ($\Delta\text{SMIM-Im}$) at different bias voltages. For both types of films, as the dc voltage is swept, $\Delta\text{SMIM-Im}$ increases and once polarization switching is complete, it starts decreasing. We observed two major differences between $\Delta\text{SMIM-Im}$ responses of the as-grown and transferred samples. Firstly, a sharp drop in $\Delta\text{SMIM-Im}$ is observed in the as-grown film, which is absent in the free-standing film. Secondly, $\Delta\text{SMIM-Im}$ during switching is higher in the as-grown film than the free-standing film.

The SMIM results suggests possible presence of strong inhomogeneous internal field distribution in free-standing films. This would cause a wide distribution of effective coercive voltages in FE unit cells. During polarization switching, a slight change in voltage (dv) creates large change in charge (dq), resulting in high capacitance (dq/dv). Before and after switching,

capacitance becomes low. Due to the difference of coercive voltages in FE cells, some switch early and some switch late. Therefore, at a certain dc voltage, only few cells under the probe provide large capacitance. Since these cells' capacitances act in parallel, effective change in total capacitance ($\sim\Delta\text{SMIM-Im}$) is low. On the contrary, internal fields in the as-grown films are more homogeneous and therefore, FE cells switch more coherently, providing large change in the $\Delta\text{SMIM-Im}$ signal. Due to the same reason, a sharp drop in $\Delta\text{SMIM-Im}$ is observed only in as-grown films.

We now consider the effect of interfacial bond-breaking on the structural properties such as lattice spacing, which is governed by the strain state of the material. During growth, PZT is under biaxial compression due to the lattice misfit with STO. Once released from the substrate, the elastic strain tends toward zero with respect to bulk PZT. Using the X-ray nanoprobe, we scanned a $2\mu\text{m} \times 2\mu\text{m}$ area, examining the line shapes of 002 Bragg reflections from the as-grown and transferred films. The average 2θ peak position is larger in the as-grown than the transferred film indicating a smaller c-axis lattice parameter – this is consistent with the expectation of a Poisson effect from an in-plane expansive release (**Figure 4a**). From this, we determine that the transferred films are 0.44% less compressively strained (in-plane) than the as-grown films. This corroborates with the slight reduction of P_s observed in the EFM studies (S4, Supporting Information).

Using these experimentally evaluated and simulated local FE properties in the Miller-Weinrich model^[22] of DW motion, we evaluate that the nominal DW energy density in the as-grown films should be larger than that in freestanding films (S4, Supporting Information). Since DWs with lower energy density should require less energy to move, the velocity is expected to increase – in direct contrast with our experimental observations. Therefore, it is clear that the variation in DW velocity between the as-grown and transferred samples cannot be attributed to the substrate-imposed epitaxial strain state modification and the associated change in FE properties. Other possibilities such as a modified electronic interface, change in epitaxy-related

strain gradient or simply increased pinning site densities are also improbable (S5, Supporting Information).

In order to further understand the local structural environment that the DWs traverse, we measured the angular dispersion of the diffraction patterns acquired near the 002 Bragg peak of PZT across a $1.5 \mu\text{m} \times 1.5 \mu\text{m}$ area, using the procedure described in the Methods section and Ref. 27. The angular shift represents tilts (τ) in the atomic planes of PZT, whose spatial distribution is plotted in Figure 4b. Within a spatial lengthscale of 200 nm, the angular displacements are found to be as large as 0.16° . Since the X-ray nanoprobe samples a volume of the film, the crystalline tilts are presumably present throughout the thickness of the film. Hence, a structural ripple with 0.5 – 1 nm height variation is possible in the freestanding films. However, this lies within the range of surface roughness of films and therefore remains undetectable in the atomic force microscope images. The tilt distribution in the transferred sample has a full-width at half-maximum of 0.096° , a factor of two larger than that for the as-grown film (Figure 4c). Similar increased tilt variation is also observed in the thicker freestanding films, confirming its origin related to the interfacial bond breaking (S6, Supporting Information).

We speculate that there is a correlation between the interfacial bond-breaking and the energy barrier for DW motion. The sudden release of the interfacial energy and strain relaxation during the transfer process can create distortion in elastic energy landscape across the thickness of the freestanding film. Unlike in Ref. 5, the thickness of the transferred layer in our case is too high for a complete melting of the crystalline order. Nevertheless, the elastic energy redistribution leaves its footprint, creating crystalline tilt and structural ripples. Figure 4d shows a representative line trace across the crystalline tilt map of the transferred sample, revealing a continuous tilt variation of different lengthscales and signs. The tilt gradient ($\partial\tau/\partial x$) is a signature of local nanoscale bending and wrinkle in the atomic planes of PZT layers, while its

sign change indicates the presence of both concave and convex-type bending. As such, a local strain difference between the bottom and top layers of PZT is developed creating a flexoelectric effect^[28-30]. According to the linear elastic theory [S7, Supporting Information], for a 1-D ripple with 200 nm wavelength and 0.55 nm height, the strain difference between the top layer and mid-plane of the film is 7×10^{-3} .^[31,32] Assuming the strain gradient – electric field coupling coefficient in PZT is ~ 75 ,^[33] we find that an additional local flexoelectric field^[34] of ~ 0.25 MV/cm can be generated in freestanding films – comparable to the coercive field of the PZT film.^[35] In fact, the ripples in freestanding films are two dimensional in space, and therefore, the strain difference between the peak and valley and the additional flexoelectric field could be much larger than what we have estimated here.

It is instructive to note that the actual flexoelectric effects at the domain walls can be more complicated than this simple scenario due to the gradual change of the order parameter. Nevertheless, such a strong flexoelectric effect in the freestanding films can increase the energy barrier for DW motion by at least a factor of two when compared to the as-grown film, as suggested by the tilt variation statistics shown in Figure 4c. As a wall moves through this highly inhomogeneous local energy landscape, it remains strongly pinned at places where the flexoelectric field is in opposite direction to the applied field. Such inhomogeneous internal field is induced in the epitaxial layers only after the transfer process, as also evident by the SMIM-Im data. This causes slowing down of the overall motion of DWs in the freestanding film. Since the DW velocity is exponentially related to the energy barrier height, a two-fold increase in flexoelectric field can lead to orders of magnitude change in velocity, particularly at the applied field range used in our experiments [S7, Supporting Information].

The flexoelectric field would be weaker in thicker freestanding films, since the wavelength of ripples linearly scales with thickness,^[36,37] which in turn should reduce the strain gradient [S7, Supporting Information]. This is why at a certain applied field, velocity difference between the as-grown and free-standing film is smaller in 100 nm thick films than that in 30

nm thick films. Therefore, DW velocity data in 100 nm thick samples further support our claim that flexoelectric effect results in the velocity difference between the as-grown and free-standing films.

In summary, this work demonstrates that the time dependent characteristics of FE DWs drastically change when epitaxially grown single-crystal complex oxide materials are made freestanding. We attribute this effect to the induced structural inhomogeneities and tilts and associated flexoelectric effects caused by the bond-breaking at the interfacial layers. In contrast, the effect of bond-breaking on the static ferroic properties, even at the bottom layers of transferred film, is very small. This is inspiring, particularly for creating electrostatically controlled devices using heterostructures containing transferred complex oxides and epitaxy-incompatible materials such as Si.

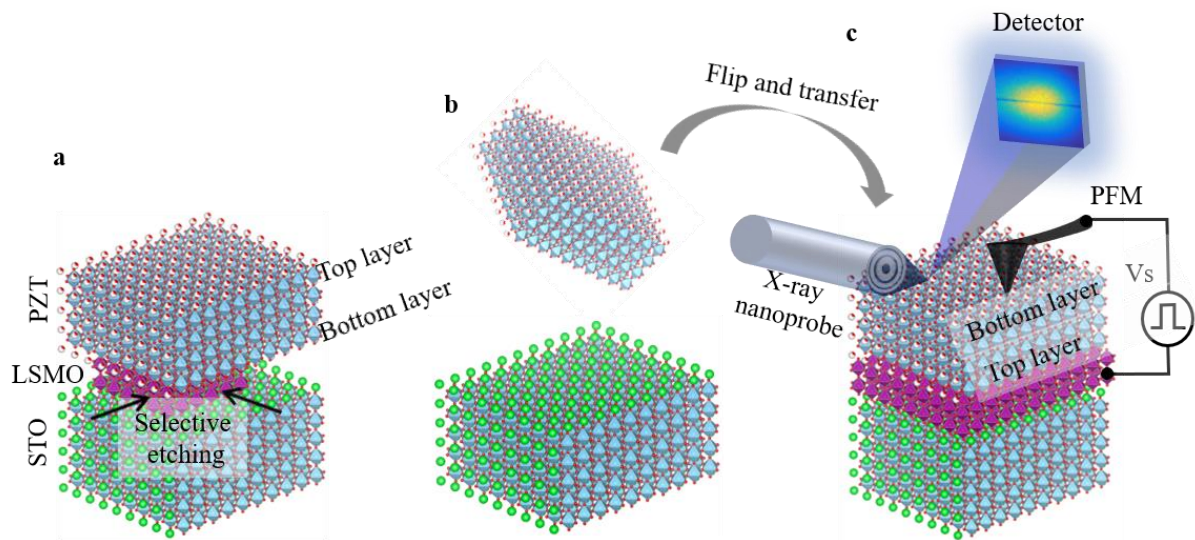


Figure 1. Scanning probe microscopy (SPM) and X-ray nanodiffraction characterization of as-grown and transferred PZT films. a) Schematic of as-grown PZT layers on sacrificial LSMO buffered STO substrate. Interfacial bonds between PZT and LSMO are broken by selectively etching LSMO layers. b) PZT layers being released from the substrate and flipped. c) Freestanding, flipped PZT layers transferred on an identical STO/LSMO substrate. Flipping the PZT layers provide direct access for characterization of bottom layers of the transferred sample. The PZT layers are scanned by SPM tip and X-ray beam, which reveal ferroelectric and structural properties with $\sim 20\text{-}30$ nm spatial resolution.

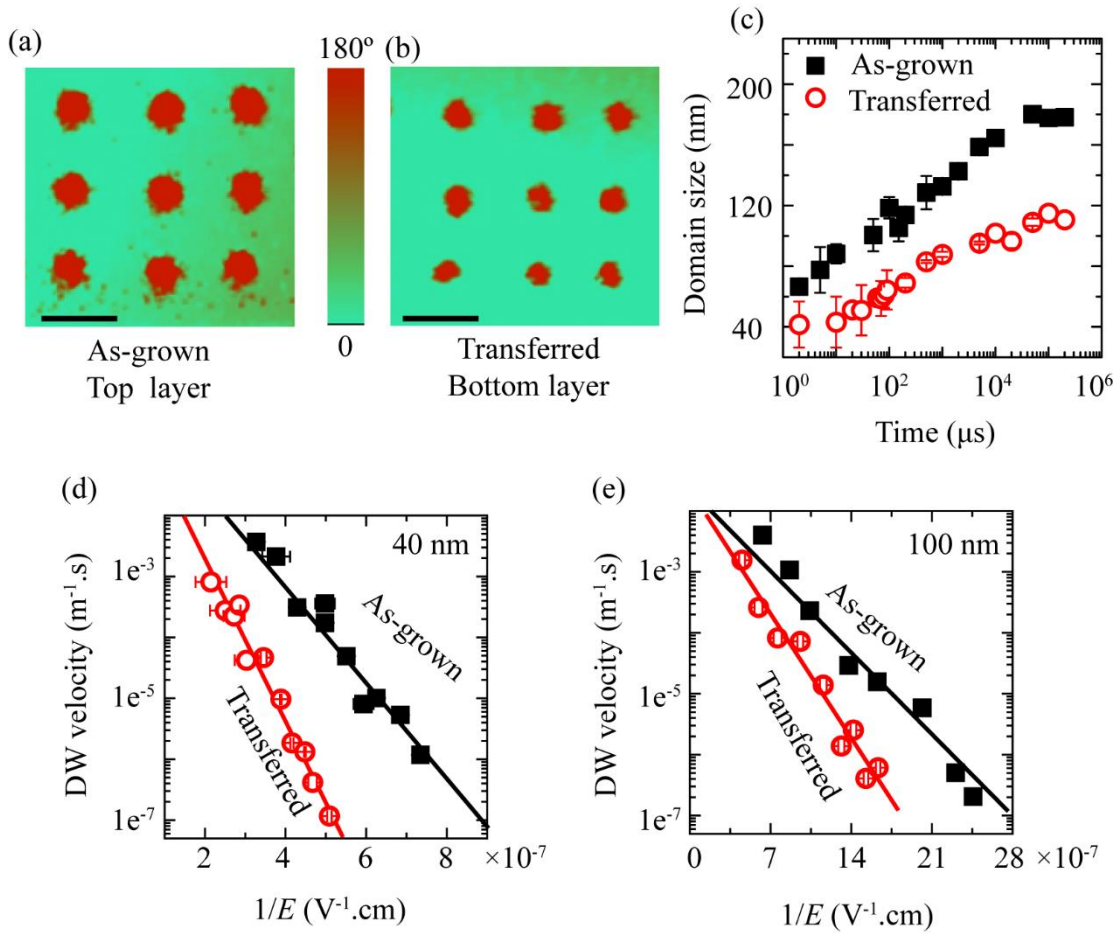


Figure 2. Domain growth and wall velocity. The scalebar is 400 nm. a, b) PFM phase contrast images captured by same probe after applying 2 ms switching pulses on pre-poled areas of the 40 nm thick as-grown film and the bottom surface of the transferred film derived from the same sample, respectively. c) Domain radius as a function of the applied electric field pulse width. d, e) Wall velocities in 40 nm and 100 nm thick as-grown and transferred films as a function of the inverse electric field. Solid lines are the fits to the law of DW creep: $v(E) \propto 1/\exp\left(\frac{E_a}{E}\right)^\mu$.
^[21,37,38] Fitting parameters are: creep exponent $\mu = 1$, effective activation field $E_a = 1.87 \times 10^7$ V/cm and 3.18×10^7 V/cm in 30 nm thick as-grown and transferred samples, respectively. In 100-nm thick samples, $E_a = 4.4 \times 10^6$ V/cm (as-grown) and 6.7×10^6 V/cm

(transferred). Note that these activation fields are derived from pulsed electric field and significantly higher than bulk static coercive field of $\sim 0.2\text{-}0.7$ MV/cm. ^[17]

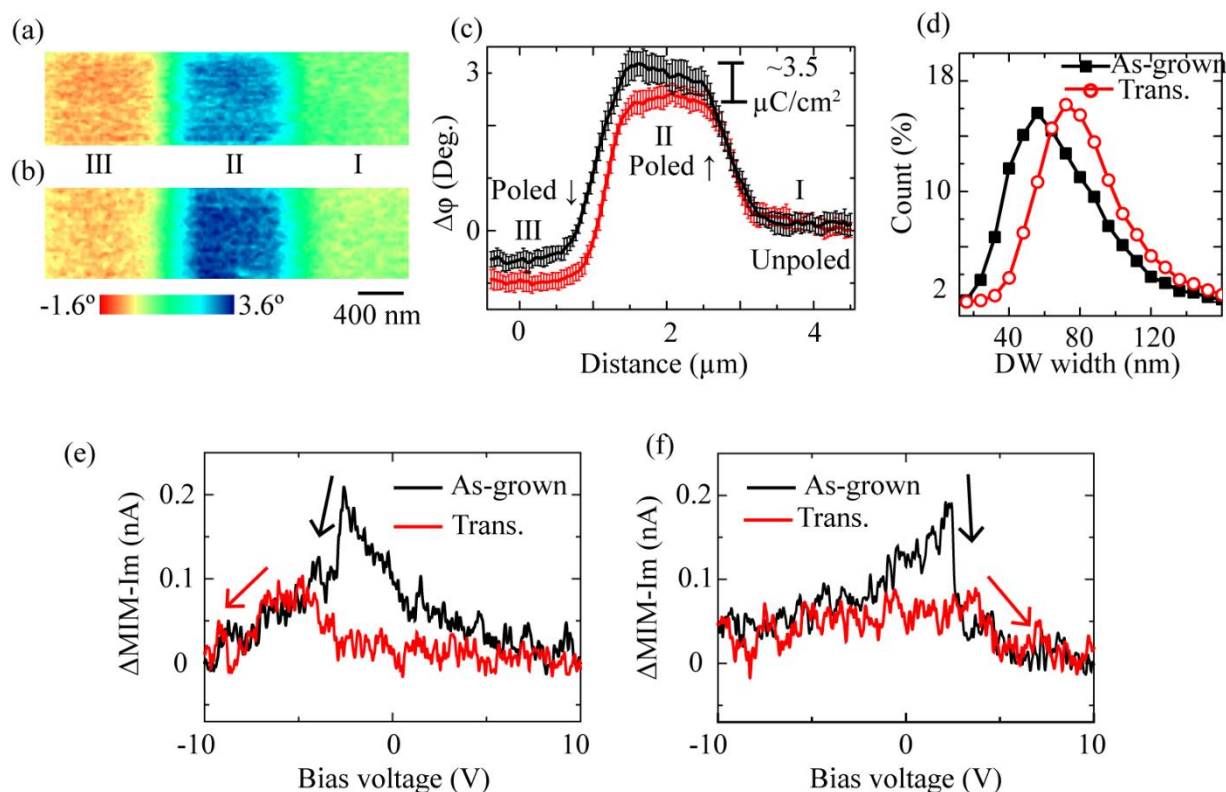


Figure 3. Static ferroelectric properties of domains and walls. The scalebar is 400 nm. a, b) EFM phase contrasts of unpoled (I), positively (II) and negatively (III) poled areas of the transferred (red) and as-grown (black) samples, respectively. c) EFM phase contrast across these three regions, averaged over different points parallel to the wall axis. For ease of comparison, signals at the unpoled areas are vertically shifted to align at the same level. d) DW widths estimated from the piezoresponse across 40 different walls (each 4-5 μm long). A total of approximately 12500-line scans have been analyzed (S3, Supporting Information), which demonstrate a tendency of widening of the DWs due to the freestanding nature of the film. e, f) SMIM (Im) signals representing change in local capacitance under dc sweeping voltage.

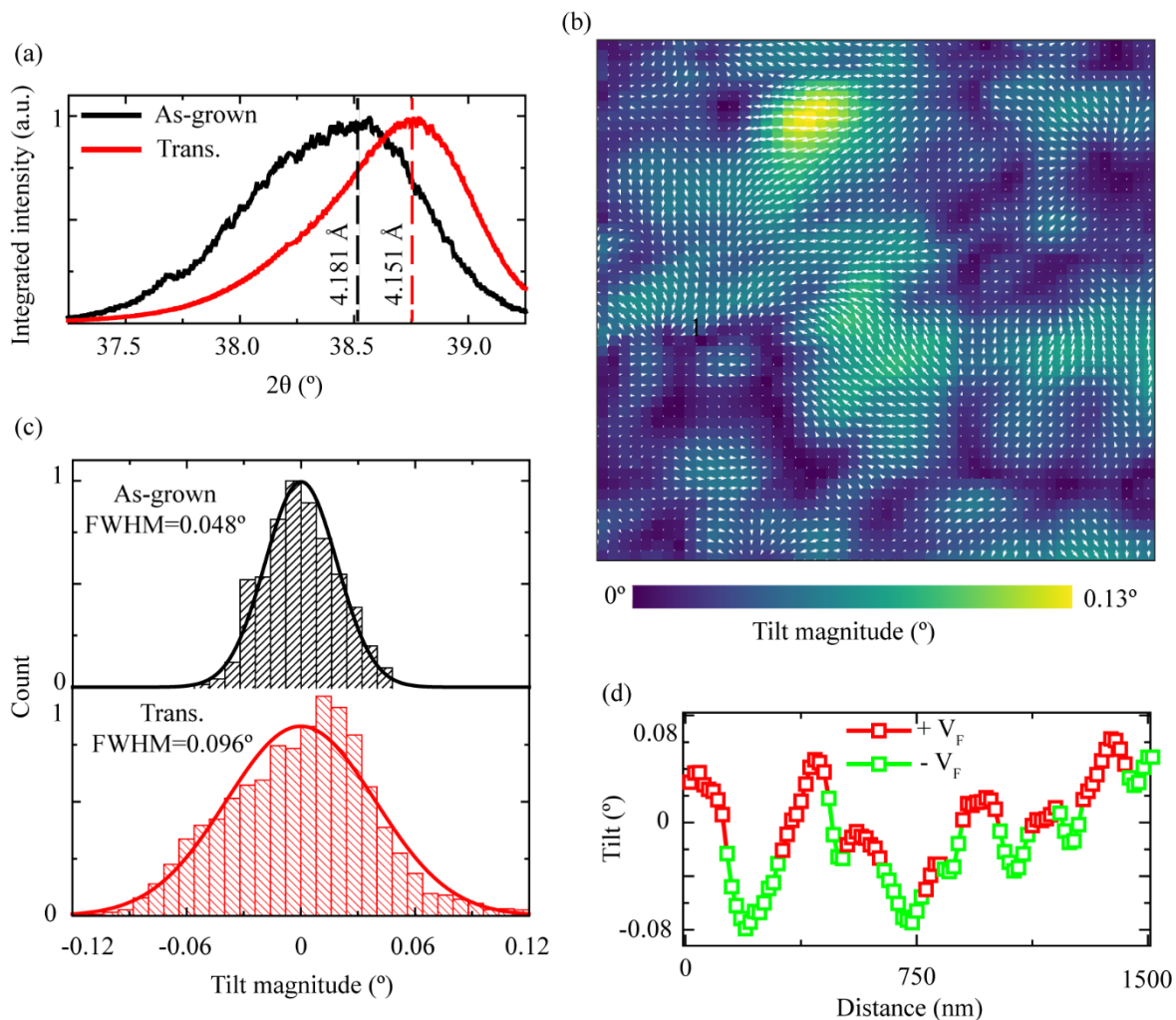


Figure 4. Nanodiffraction data from the as-grown and transferred films. a) $\theta - 2\theta$ line scans around the (002) reflection averaged over $2 \times 2 \mu\text{m}^2$ area. b) Map of crystallographic tilts in a $1.5 \times 1.5 \mu\text{m}^2$ area of the transferred PZT. Arrows indicate local tilt directions. Continuous variation of crystallographic tilt represents local nanoscale bending of atomic planes and the presence of inhomogeneous, built-in electric field due to the flexoelectric effect. c) Histograms representing the variations in tilt magnitudes. After PZT is made freestanding, the tilt variation is significantly enhanced. d) A line profile of the crystallographic tilt map, showing both concave and convex-type bending are present. Places with opposite flexoelectric field directions are colored in red and green.

Experimental Section

Sample preparation: 40 nm thick $\text{Pb}_{0.8}\text{Zr}_{0.2}\text{TiO}_3$ films are epitaxially grown at 700 °C on 10 nm thick $\text{La}_{0.7}\text{Sr}_{0.3}\text{MnO}_3$ (LSMO) buffered SrTiO_3 substrate using pulsed laser deposition technique. LSMO acts as a sacrificial layer, which is wet etched using KI solution to make the PZT layers freestanding. The layers are subsequently collected using Polymethyl (PMMA) stamps, flipped over and transferred onto another identical LSMO/STO substrate. The PMMA stamp is then removed by acetone. Flipping of the PZT/PMMA assembly provides direct access to the interfacial layers and facilitates imaging of these layers using SPM techniques. More details about the sample preparation can be found in Ref. 3 and Ref. 4.

Scanning Microwave impedance microscopy: A 3 GHz signal of 100 μW (-10dBm) is delivered to the sample through a metallic AFM probe.^[15] The same probe is used to capture reflected signal amplitude and phase. The real (SMIM-Re) and imaginary (SMIM-Im) part of the reflected signal correspond to the resistive and capacitive behavior of the tip-sample complex admittance. A sweeping (± 10 V) dc voltage was superimposed with the microwave signal to bias the ferroelectric material.

X-ray nanodiffraction: Comparison of c-axis strain observed using the Bragg diffraction line shape from the 002 reflection of as-grown and freestanding thin films was made using focused 9keV x-rays at the CNM/APS Hard X-ray Nanoprobe. The spot size of the focused x-ray beam was 20-30 nm full width at half-maximum. The outgoing diffraction signal was resolved in scattering angle (2θ) by a pixel array detector with $55 \mu\text{m} \times 55 \mu\text{m}$ pixels positioned 800mm away from the sample/beam intersection giving 0.004° angular sampling. This signal was summed over a 2° rocking curve (sample rotation made relative to the incident beam) in 0.1° steps about the observed maximum intensity. Such data were taken from different places of a $2 \mu\text{m} \times 2 \mu\text{m}$ area and the averaged results are shown in Figure 4a. The local crystalline tilt is

mapped by varying the position of the beam on the sample under a fixed 2θ angle and observing the shift of the center of mass in the axes parallel ($X - tilt$) and perpendicular ($Y - tilt$) to the scattering plane. In Figure 4b the arrows indicate an angle corresponding to $\tan^{-1}(Y - tilt / X - tilt)$ and the magnitudes represent $\sqrt{(X - tilt)^2 + (Y - tilt)^2}$. In all cases the synchrotron x-ray beam was focused onto the sample using a Fresnel zone plate optic creating a common 0.3° angular divergence observed in each line shape.

Estimation of DW velocity: We have estimated the lateral velocity of the walls as $v(E) = \frac{R(t_1) - R(t_2)}{t_1 - t_2}$ and lateral electric field as $E = \frac{V}{R(t_1) - R(t_2)}$.^[17] Here, $R(t)$ is the domain radius, which is a function of the pulsewidth (t). As the wall velocity strongly depends on the characteristic timescale of the measurement,^[38] it has been calculated from two successive pulses with widths of similar order of magnitude ($\frac{t_2}{t_1} \sim 3 - 5$).

Supporting Information

Supporting Information is available from the Wiley Online Library or from the author.

Acknowledgements

Scanning probe microscopy, electronic transport and sample fabrication carried out at Argonne National Laboratory was supported by the US Department of Energy, Office of Basic Energy Sciences, Materials Sciences and Engineering Division. Use of the Center for Nanoscale Materials was supported by the US Department of Energy, Office of Science, Office of Basic Energy Sciences, under contract no. DE-AC02-06CH11357. Materials growth carried out at University of California Berkeley was supported by Office of Naval Research Contract No: N00014-14-1-0654. J. K. and S. H. acknowledge support from Brain Korea 21 Plus and KAIST. We acknowledge Prof. Ramamoorthy Ramesh and Prof. Paul Evans for helpful discussions.

Received: ((will be filled in by the editorial staff))
Revised: ((will be filled in by the editorial staff))
Published online: ((will be filled in by the editorial staff))

References

- [1] S. Manipatruni, D. E. Nikonov, I. A. Young, *Nat. Phys.* **2018**, *14*, 338.
- [2] J. Levy, *Phys. Rev. A* **2001**, *64*, 7.
- [3] S. R. Bakaul, C. R. Serrao, O. Lee, Z. Lu, A. Yadav, C. Carraro, R. Maboudian, R. Ramesh, S. Salahuddin, *Adv. Mater.* **2017**, *29*, 1605699.
- [4] S. R. Bakaul, C. R. Serrao, M. Lee, C. W. Yeung, A. Sarker, S. L. Hsu, A. K. Yadav, L. Dedon, L. You, A. I. Khan, J. D. Clarkson, C. Hu, R. Ramesh, S. Salahuddin, *Nat. Commun.* **2016**, *7*, 10547.
- [5] S. S. Hong, J. H. Yu, D. Lu, A. F. Marshall, Y. Hikita, Y. Cui, H. Y. Hwang, *Sci. Adv.* **2017**, *3*, eaao5173.
- [6] D. Lu, D. J. Baek, S. S. Hong, L. F. Kourkoutis, Y. Hikita, H. Y. Hwang, *Nat. Mater.* **2016**, *15*, 1255.
- [7] L. Shen, L. Wu, Q. Sheng, C. Ma, Y. Zhang, L. Lu, J. Ma, J. Ma, J. Bian, Y. Yang, A. Chen, X. Lu, M. Liu, H. Wang, C. L. Jia, *Adv. Mater.* **2017**, *29*, 1702411.
- [8] D. M. Paskiewicz, R. S.-Tissot, E. Karapetrova, L. Stan, D. D. Fong, *Nano Lett.* **2016**, *16*, 534.
- [9] Z. Chen, B. Y. Wang, B. H. Goodge, D. Lu, S. S. Hong, D. Li, L. F. Kourkoutis, Y. Hikita, and H. Y. Hwang, *Phys. Rev. Mater* **2019**, *3*, 060801(R).
- [10] D. Ji, S. Cai, T. R. Paudel, H. Sun, C. Zhang, L. Han, Y. Wei, Y. Zang, M. Gu, Y. Zhang, W. Gao, H. Huyan, W. Guo, D. Wu, Z. Gu, E. Y. Tsymbal, P. Wang, Y. Nie, X. Pan, *Nature* **2019**, *570*, 87.
- [11] M. P. Warusawithana, C. Cen, C. R. Slesman, J. C. Woicik, Y. Li, L. F. Kourkoutis, J. A. Klug, H. Li, P. Ryan, L. Wang, M. Bedzyk, D. A. Muller, L. Chen, J. Levy, D. G. Schlom, *Science* **2009**, *324*, 367.
- [12] M. Lalart, *Ferroelectrics – Applications*, Intech, Rijeka, Croatia **2011**.

- [13] S. Hong, J. Woo, H. Shin, J. U. Jeon, Y. E. Pak, E. L. Colla, N. Setter, E. Kim, and K. No, *J. Appl. Phys.* **2001**, *89*, 1377.
- [14] S. Tong, I. W. Jung, Y.-Y. Choi, S. Hong, and A. Roelofs, *ACS Nano* **2016**, *10*, 2568.
- [15] A. Tselev, P. Yu, Y. Cao, L. Dedon, L. Martin, S. Kalinin, P. Maksymovych, *Nat. Commun.* **2016**, *7*, 11630.
- [16] M. Holt, R. Harder, & V. Rose, *Annu. Rev. Mater. Res.* **2013**, *43*, 183.
- [17] T. Tybell, P. Paruch, T. Giamarchi, J. M. Triscone, *Phys. Rev. Lett.* **2002**, *89*, 097601.
- [18] P. Paruch, T. Giamarchi, J. Triscone, *Phys. Rev. Lett.* **2005**, *94*, 197601.
- [19] W. J. Merz, *Phys. Rev.* **1954**, *95*, 690.
- [20] J. Y. Jo, S. M. Yang, T. H. Kim, H. N. Lee, J. Yoon, S. Park, Y. Jo, M. H. Jung, T. W. Noh, *Phys. Rev. Lett* **2009**, *102*, 045701.
- [21] E. Guo, R. Roth, A. Herklotz, D. Hesse, K. Dörr, *Adv. Mater.* **2015**, *27*, 1615.
- [22] R. C. Miller, G. Weinreich, *Phys. Rev.* **1960**, *117*, 1460.
- [23] N. A. Pertsev, V. G. Kukhar, H. Kohlstedt, R. Waser, *Phys. Rev. B* **2003**, *67*, 054107.
- [24] C. H. Lei, A. Das, M. Elliott, J. E. Macdonald, *Nanotechnology* **2004**, *15*, 627.
- [25] B. L. Chang, M. Alexe, J. F. Scott, J. M. Gregg, *Adv. Mater.* **2009**, *21*, 4911.
- [26] M. Stengel, N. A. Spaldin, *Nature* **2006**, *443*, 679.
- [27] P. G. Evans, D. E. Savage, J. R. Prance, C. B. Simmons, M. G. Lagally, S. N. Coppersmith, M. A. Eriksson, T. U. Schüllli, *Adv. Mater.* **2012**, *24*, 5217.
- [28] D. Lee et al., *Phys. Rev. Lett.* **2011**, *107*, 057602.
- [29] H. Lu et al., *Science* **2012**, *336*, 59.
- [30] P. Zubko, G. Catalan, A. K. Tagantsev, *Annu. Rev. Mater. Res.* **2013**, *43*, 387.
- [31] D. Vella, J. Bico, A. Boudaoud, B. Roman, P. M. Reis, *PNAS* **2009**, *106*, 10901.
- [32] A. Castellanos-gomez, R. Rolda, E. Cappelluti, M. Buscema, *Nano Lett.* **2013**, *13*, 5361.
- [33] W. Ma, *Phys. Stat. Sol.* **2008**, *768*, 761.
- [34] P. Zubko, G. Catalan, A. K. Tagantsev, *Annu. Rev. Mater. Res* **2013**, *43*, 387.

[35] From Figure 3d and 3e, local dc coercive field can be estimated as 0.25-0.7 MV/cm. This field is more than one order smaller than the activation field derived from the velocity vs. pulsed electric field data. This is understandable, since energy transferred to the system to overcome the energy barrier depends on the duration of the applied field. Similar difference between dc and pulsed coercive fields is also reported in Ref. 17.

[36] S. Deng and V. Berry, *Materials Today* **2016**, *19*, 197.

[37] E. Cerda and L. Mahadevan, *Phys. Rev. Lett.* **2003**, *90*, 074302.

[38] J. Y. Jo, S. M. Yang, T. H. Kim, H. N. Lee, J. Yoon, S. Park, Y. Jo, M. H. Jung, T. W. Noh, *Phys. Rev. Lett* **2009**, *102*, 045701.

[39] Q. Meng, M. Han, J. Tao, G. Xu, D. O. Welch, Y. Zhu, *Phys. Rev. B* **2015**, *91*, 054104.

Copyright WILEY-VCH Verlag GmbH & Co. KGaA, 69469 Weinheim, Germany, 2018.

Supporting Information

Ferroelectric domain wall motion in freestanding single-crystal complex oxide thin film

*Saidur R. Bakaul**, Jaegy Kim, Seungbum Hong, Mathew J. Cherukara, Tao Zhou, Liliana Stan, Claudy R. Serrao, Sayeef Salahuddin, Amanda K. Petford-Long, Dillon D. Fong, Martin V. Holt

S1. Domain wall motion in the top layers of transferred PZT

Figure S1 shows the domain size and estimated domain wall velocity evaluated at the top surface of the transferred sample. Same tip was used to collect all the data of Figure S1. To avoid any effect of longer pulses on the probe size and associated artifacts, separate probes were used for the experiments on the as-grown and transferred sample. However, all data on one type

of sample were taken by the same tip. Moreover, same sequence of pulse width increment was used for all samples. In addition, same applied force was used for all measurements.

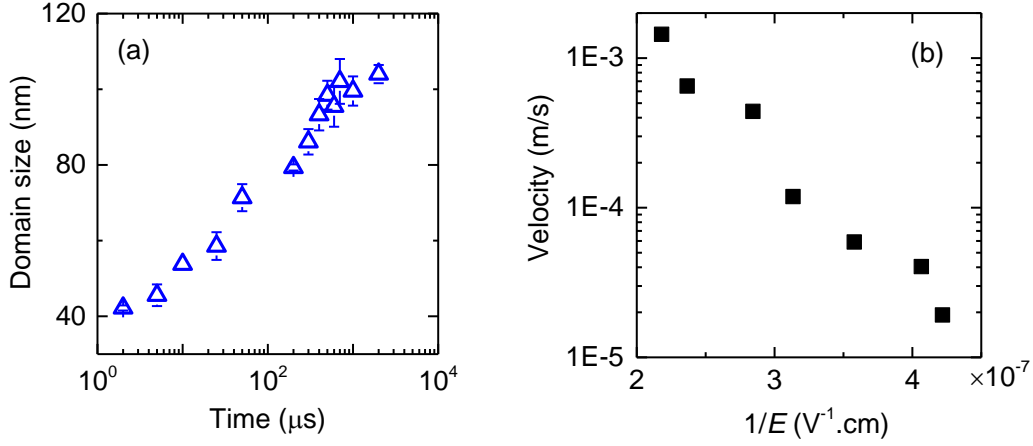


Fig S1. a, b) Domain sizes and velocity at the top surface of the transferred PZT sample.

S2. Estimation of surface charge density:

To measure surface charge density (P_s), we created up- and down-polarized regions using ± 8 V and measured the electrostatic force microscopy (EFM) phase contrast in those areas. The phase shift between two oppositely poled areas is φ and the difference between φ in transferred sample and as-grown sample is

$$\Delta\varphi \propto \sin^{-1}\{A \cdot (V_{tip} - V_{surface})^2\}$$

Here, A is a constant that depends on the tip parameter and imaging configuration such as, tip-sample height difference and stray capacitances, which remained same throughout the EFM experiments. $\Delta\varphi = 0.4^\circ$, $V_{tip} = 1$ V, tip diameter = 20 nm and tip-sample distance = 50 nm.

From these values we determine the ratio of surface charge densities ($\frac{P_{S-trans.}}{P_{S-as-grown}}$) in the transferred and as-grown samples as 0.9412. Since the relationship between P_s and strain is quadratic, ($strain(X) = Q \cdot P^2$), and from X-ray diffraction we know a 0.44% change in strain occurred due to transfer process, theoretically, $\frac{P_{S-trans.}}{P_{S-as-grown}}$ is expected to be around

0.89, which is very close to the value obtained from the EFM studies. Here, $Q=0.08$ is the electrostrictive coefficient, calculated from the empirical relationships^[1] with Ti:Zr ratio.

S3. Domain wall (DW) width:

To characterize DW widths (W), we measured piezoforce microscopy (PFM) amplitude across 30 separate, artificially written (each 3-4 μm long) DWs in each type of sample. The PFM amplitude goes to near zero in the middle of the DW. We took the spatial distance between two points on the two sides of the DW where PFM amplitude reaches 80% of the saturation value. We note that the DW width measured by the PFM could be exaggerated due to the tip-surface convolution effect. However, a comparative study can be performed when statistically averaged data from the same tip are used.^[2] We have analyzed approximately 12500 line scans across 40 different DWs and plotted the percentage of walls with certain width (Figure 3d in main text). Clearly, the peak of the percentage of walls vs. DW width curve shift towards right after the transfer process. This has led us to the claim that there is a tendency of slight increase in the DW width after transfer process. The mean DW widths from these analyses have been found to be 56 and 72 nm in the as-grown and transferred samples, respectively. Although these values could be one order higher than that obtained from the transmission electron microscopy experiments, this does not alter our main claim that the change in strain and possible change in DW energy density are unable to explain DW velocity reduction in freestanding films.

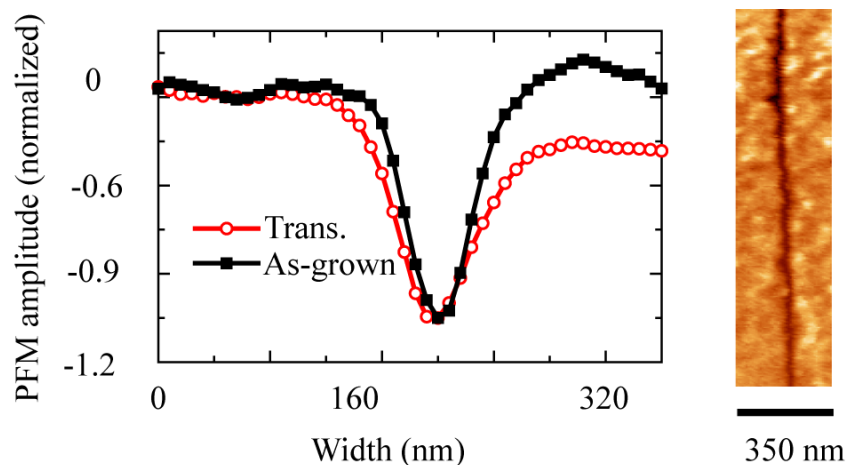


Figure S2. Piezoresponse across a domain wall.

S4. DW and domain energy densities:

DW energy consists of two terms – one stems from the ferroic ordering and the other is related to the gradient of order parameter.^[3] The total energy density of a DW is:

$\sigma_W = 2k \frac{P_S^2}{W} + \frac{1}{6} \chi^{-1} P_S^2 W$. Here, $K = 1 \times 10^{-10}$ Coul⁻².m⁴.N is the gradient coefficient for PZT, ^[4] P_S is polarization, W is DW wall width and χ is susceptibility. Since $W \propto \sqrt{\chi}$, we can easily deduce a wall energy expression independent of the wall width: $\sigma_W \propto 2k \frac{P_S^2}{\sqrt{\chi}} + \frac{1}{6} \frac{P_S^2}{\sqrt{\chi}}$.

Since measurement of the local susceptibility is beyond our instrumentation capability, we estimate it using its theoretical dependence on the experimentally evaluated strain information. The constants and formula used here can be found in the Supporting Information references 1,5,6. For PbZr_{0.2}Ti_{0.8}O₃, assuming that the freestanding layers are nominally strain free, using empirical relationship with Ti:Zr ratio, we can calculate the Curie-Weiss coefficient

$$C_0 = \frac{2.8339}{1 + 126.56(0.8 - 0.5)^2} + 1.4132) \times 10^5 = 1.642 \times 10^5$$

Change in T_c due to the change in strain $\Delta T_c = 2\epsilon_0 C_0 \frac{Q_{11}+Q_{12}}{S_{11}+S_{12}} \cdot \Delta Strain$ (in – plane)

Q_{ij} and S_{ij} are electrostrictive coefficients and elastic compliances, respectively.

$$Q_{11} = \frac{0.029578}{1 + 200(0.8 - 0.5)^2} + 0.0428 \times 0.8 + 0.045 \approx 0.081 \text{ Coul}^{-2} \cdot \text{m}^4$$

$$Q_{12} = \frac{0.026}{1 + 200(0.8 - 0.5)^2} + 0.012 \times 0.8 - 0.01 \approx -0.002 \text{ Coul}^{-2} \cdot \text{m}^4$$

$$S_{11} = 8.2 \times 10^{-12} \text{ m}^2/\text{N}$$

$$S_{12} = -2.6 \times 10^{-12} \text{ m}^2/\text{N}$$

In-plane strain change:

$$\frac{\Delta c}{c} = -\frac{2\nu}{1-\nu} \cdot \frac{\Delta a}{a}$$

c and a are out-of-plane and in-plane lattice constants, respectively. $\nu=0.46$ is the Poisson coefficient. From experimentally evaluated out-of-plane lattice constants we can estimate change in in-plane strain is 4.4×10^{-3} . Therefore, difference between T_c of the as-grown and freestanding film is 179.1 K.

Since the freestanding film is close to strain-free state, we calculate T_c for this case using empirical formula ($x = 0.8$):

$$T_{c_1} = 462.63 + 843x - 2105.5x^2 + 4041.8x^3 - 3828.2x^4 + 1337.8x^5 = 729.53\text{K}$$

$$\chi_1 = \frac{\epsilon_0 C_0/2}{-T + T_{c_1}} = 1.69 \times 10^{-9}$$

In the as-grown film, $T_{c_2} = 908.6\text{ K}$, $\chi_2 = 1.19 \times 10^{-9}$.

Experimental results show that the spontaneous polarization in the freestanding films is $3 \pm 2 \mu\text{C}/\text{cm}^2$ lower than the as-grown films. Since in freestanding films, polarization reduces and susceptibility increases, DW energy must be reduced.

According to the Miller-Weinrich model, DW velocity $\propto \exp - \left(\frac{8b}{3\sqrt{3}} \cdot \frac{\sigma_p^{\frac{1}{2}} \cdot \sigma_p^{\frac{3}{2}}}{P_s EKT} \right)$. Here,

$\sigma_p = \frac{4P_s^2 b \ln(\frac{2a^*}{eb})}{\epsilon_r}$ is the energy of new domain, $a^* = \frac{2}{3} \cdot \frac{\sigma_W}{P_s E}$, E is the applied field and K is the

Boltzman constant. Clearly, σ_p should also reduce in the freestanding film. All together, considering possible changes in DW and domain properties, the wall velocity in the freestanding film should be increase, which is opposite to the experimental observations.

S5. Alternative explanations of DW velocity reduction:

A possible explanation of the DW velocity change might be the presence of a constant voltage drop due to the modified electronic interface between the bottom layer and the substrate or an additional built-in voltage due to the substrate-induced homogeneous strain gradient. However,

we discard these possibilities since according to Merz’s law such a constant additional voltage drop would result in a parallel shift in the v vs. $1/E$ characteristics, whereas we observe a slope change. Moreover, substrate induced strain-gradient should result in a voltage with polarity opposite to the applied voltage, and hence lower the DW velocity in the as-grown samples compared to the transferred samples, which is in contrast to the experimental observation.

In addition, DW motion is strongly correlated to atomic-scale disorder and defects that creates random pinning potentials for a moving interface. A measure that provides statistical information about such pinning sites is the scaling behavior analysis of static DW surfaces.^[7,8] At equilibrium, DWs can be treated as elastic manifolds immobilized at randomly distributed, quenched pinning centers originating from two universal classes of disorders- random field and random bond type. The strength or density of pinning sites is reflected by the DW surface roughness $B(L) = L^{2\zeta}$ where L is the spatial length scale and ζ is the roughness exponent. From fitting of this power law relationship, we estimate the average ζ for the as-grown and freestanding samples to be 0.23 ± 0.05 and 0.21 ± 0.05 , respectively (Figure S5). The insignificant variance of DW roughness between the as-grown and transferred films indicates that the defect densities remain in the same order and cannot be responsible for the huge difference of DW speed between the two types of samples.

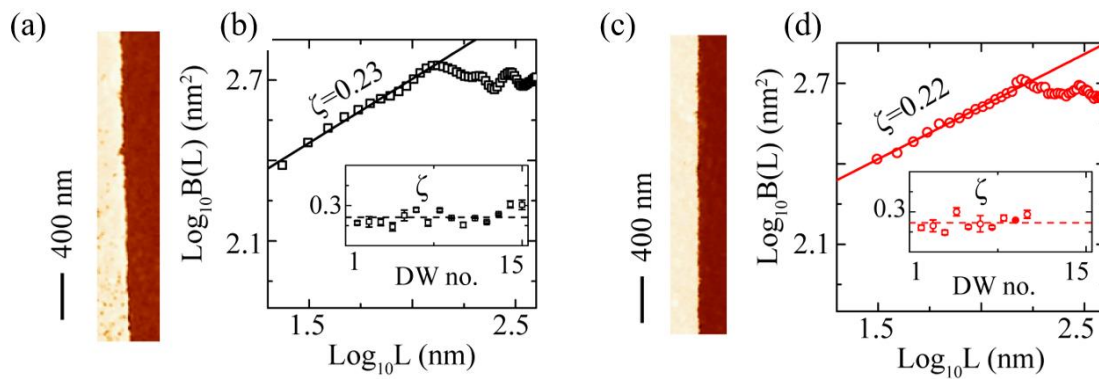


Figure S3. Displacement correlation function $B(L)$ as a function of lengthscale L for a, b) the as-grown film and c, d) the transferred film. DW roughness exponents are found by fitting the linear portions of $B(L)$ - L data.

S6. Crystalline tilt variation:

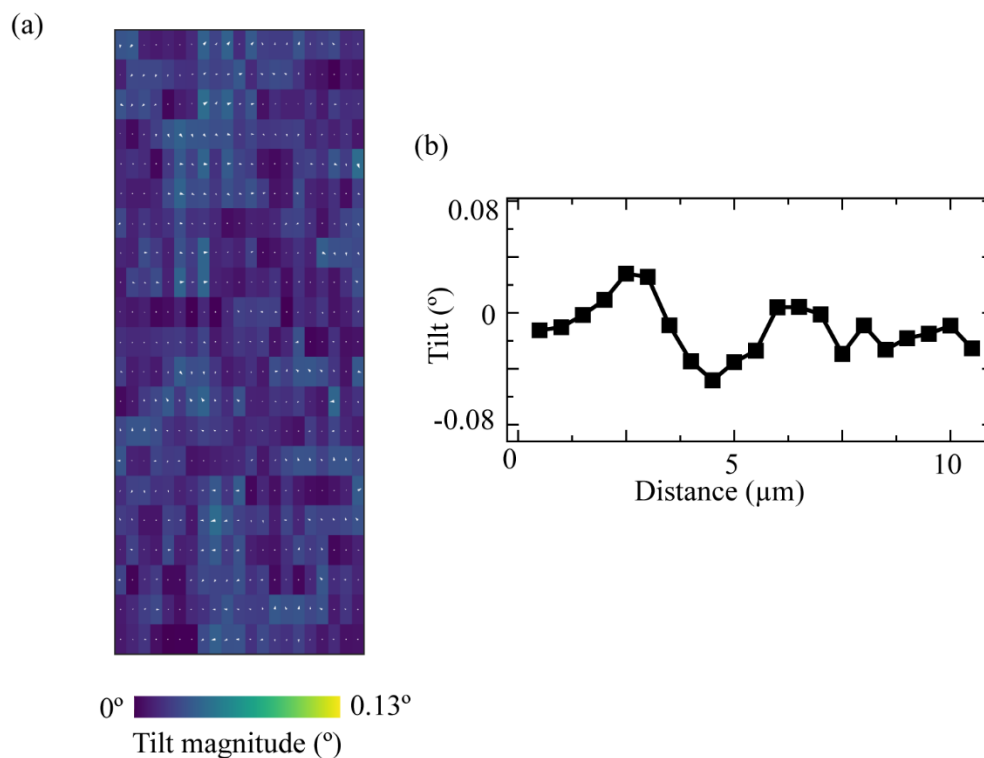


Figure S4. a) Map of crystallographic tilts in a $2.5 \times 10 \mu\text{m}^2$ area of the 40 nm thick, as-grown PZT. b) A representative line profile of the crystallographic tilt map.

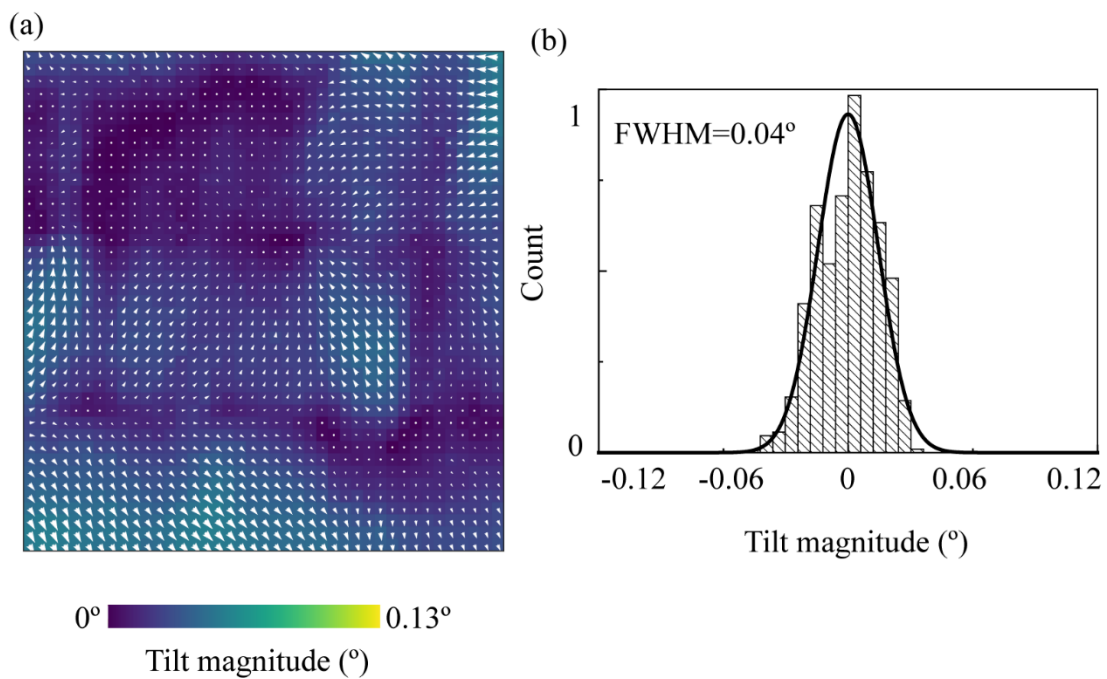


Figure S5. a) Map of crystallographic tilts in a $1 \times 1 \mu\text{m}^2$ area of the 100 nm thick as-grown PZT. b) Histograms representing the variations in tilt magnitudes.

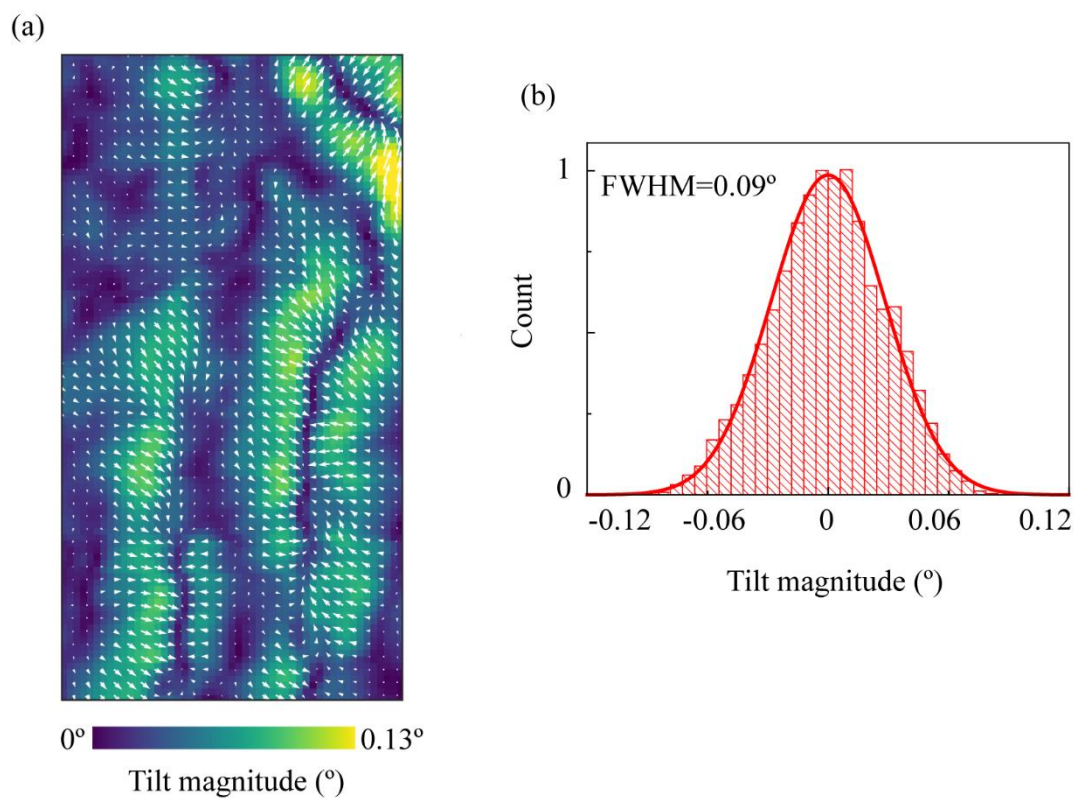


Figure S6. a) Map of crystallographic tilts in a $1 \times 1.8 \mu\text{m}^2$ area of the 100 nm thick transferred PZT. b) Histograms representing the variations in tilt magnitudes.

S7. Estimation of flexoelectric field due to strain gradient and its effect on DW velocity:

Maximum strain that can be generated at the top of a wrinkled free-standing thin film is:

$$S = \frac{\pi^2 h \delta}{(1-\theta^2)\lambda^2} \approx 7 \times 10^{-3}. \quad [10]$$

Here,

δ = Maximum height of a wrinkle = 0.55 nm (Assuming maximum tilt of 0.16° and

λ = width of the wrinkle.= 200 nm)

h = Free-standing film thickness = 40 nm

Considering top and bottom layers have concave and convex bending respectively, estimated strain gradient ∇S is 3.5×10^5 /m. The generated flexoelectric field can be estimated as:

$$E_{Flex} = 2\Phi_{12} \times \nabla S = 5.25 \times 10^5 \text{ V/cm.}$$

Here, strain gradient-electric field coupling coefficient (V) $\Phi_{12} \approx 75 \text{ V}$ [11]. This is the excess internal electric field that can be generated by making the films freestanding.

Since the DW velocity is an exponential function of the E_a/E ratio, it strongly depends on the applied electric field range and can be changed by orders of magnitude by a two-fold change of E_a in an appropriate range of $1/E$. This is also evident by the fact that at a certain field, DW velocity is orders of magnitude higher in thicker films compared to the thinner films, whereas activation energy in two cases differ by only 2-3 times (Main text Figure 2d and Supplementary Ref.12).

Supplementary References

- [1] K. M. Rabe, C. Ahn, J.-M. Triscone, *Physics of Ferroelectrics*, Springer, Heidelberg, **2007**.
- [2] V. Gopalan, V. Dierolf, D. A., Scrymgeour, *Annu. Rev. Mater. Res* **2007**, *37*, 449.
- [3] G. Catalan, J. Seidel, R. Ramesh, J. F. Scott, *Rev. Mod. Phys.* **2012**, *84*, 119.
- [4] T. M. J. Haun, Z. Q. Zhuang, E. Furman, S. J. Jang, and L. E. Cross, *Ferroelectrics* **1989**, *99*, 45.
- [5] Y. Daia, J. Schubert, E. Hollmann, G. Mussler, and R. Wördenweber, *J. Appl. Phys.* **2016**, *120*, 114101.
- [6] R. C. Miller, G. Weinreich, *Phys. Rev.* **1960**, *117*, 1460.
- [7] G. Blatter, M. V. Feigelman, V. B. Geshkenbein, A. I. Larkin, V. I. Vinokur, *Rev. Mod. Phys.* **1994**, *66*, 1125.
- [8] J. Guyonnet, *Ferroelectric Domain Walls*, Springer, Switzerland, **2014**.
- [9] R. Roldán, A. Castellanos-Gomez, E. Cappelluti, and F. Guinea, *J. Phys.: Condens. Matter.* **2015**, *27*, 313201.
- [10] D. Vella, J. Bico, A. Boudaoud, B. Roman, P. M. Reis, *PNAS* **2009**, *106*, 10901.
- [11] W. Ma, *Phys. Stat. Sol.* **2008**, *768*, 761.
- [12] T. Tybell, P. Paruch, T. Giamarchi, J. M. Triscone, *Phys. Rev. Lett.* **2002**, *89*, 097601.